Butterfly effect and a self-modulating El Niño response to global warming

Wenju Cai[1,2*], Benjamin Ng[2], Tao Geng[1,2], Lixin Wu[1*], Agus Santoso[2,3], Michael J. McPhaden[4]

[1]Key Laboratory of Physical Oceanography–Institute for Advanced Ocean Studies, Ocean University of China and Qingdao National Laboratory for Marine Science and Technology, Yushan Road, Qingdao 266003, China.

[2]Centre for Southern Hemisphere Oceans Research (CSHOR), CSIRO Oceans and Atmosphere, Hobart 7004, Australia.

[3]Australian Research Council (ARC) Centre of Excellence for Climate Extremes, Level 4 Mathews Building, The University of New South Wales, Sydney 2052, Australia.

[4]NOAA/Pacific Marine Environmental Laboratory, Seattle, WA 98115, USA.

*Correspondence to: Wenju Cai (Email: Wenju.cai@csiro.au), or Lixin Wu (E-mail: lxwu@ouc.edu.cn)

El Niño and La Niña, collectively referred to as El Niño-Southern Oscillation (ENSO), are not only highly consequential[1-6] but also strongly nonlinear[7-14]. For example, maximum warm anomalies of El Niño, which occur in the equatorial eastern Pacific Ocean, are larger than maximum cold anomalies of La Niña, which centre in the equatorial central Pacific[7,8,9]. The associated atmospheric nonlinear thermal damping cools the equatorial Pacific during El Niño but warms during La Niña[15,16]. Under greenhouse warming, climate models project an increase in frequency of strong El Niños and La Niñas, but the change differs vastly across models[17], partially attributed to internal variability[18-23]. Here we show that an infinitesimal random perturbation to an identical initial condition, like a butterfly effect[24], induces vastly different initial ENSO variability, which systematically affects its response to greenhouse warming a century later. In experiments with higher initial variability, a greater cumulative oceanic heat loss from ENSO thermal damping reduces stratification of the upper equatorial Pacific Ocean, leading to a smaller increase in ENSO variability under greenhouse warming. This self-modulating mechanism operates in two large ensembles with two models each commencing from an identical initial condition but with a butterfly perturbation, in a large ensemble with another model commencing from different initial conditions[27,28], and across climate models participating in the Coupled Model Inter-comparison (CMIP) projects[29,30]. Thus, greenhouse warming-induced increase in ENSO variability[31], if suppressed initially by internal variability, is likely to enhance in the future, and vice-versa. This self-modulation linking ENSO variability

across time presents a novel perspective for understanding dynamics of ENSO variability on multiple timescales and in a changing climate.

Main text

El Niño and La Niña events affect extreme weather, ecosystems, and food production worldwide[1,2], but their impacts are highly asymmetric. For example, during the strong 1997 El Niño event, anomalously high sea surface temperatures (SSTs) occurred in the equatorial eastern Pacific, inducing floods in the equatorial eastern Pacific regions of Ecuador and northern Peru[1,2], and equatorward movement of the Intertropical Convergence Zone and the South Pacific Convergence Zone leading to catastrophic floods and droughts across the Pacific[31]. However, during the strong 1998 La Niña, maximum cold anomalies occurred in the equatorial central Pacific[8,12], leading to intense atmospheric convection in the western Pacific which caused catastrophic river floods[3], severe food shortages, and the spread of water-borne epidemic diseases[4,5].

This asymmetric impact is governed by nonlinear ENSO dynamics, manifested as Eastern Pacific (EP) and Central Pacific (CP) ENSO regimes, characterised by an SST anomaly centre in the equatorial eastern and central Pacific, respectively[8]. During CP El Niño, eastward displacement of western Pacific atmospheric deep convection is limited, and anomalous eastward oceanic advection of warm water dominates[32,33]. During CP La Niña, a shallower than normal equatorial thermocline in the central Pacific, typically due to heat discharge from a prior EP El Niño, facilitates the fast growth of cold anomalies, contributing to negative SST skewness there[34]. In the normally cold and dry eastern Pacific, cool anomalies are curtailed by a limited upward displacement of the shallow climatological mean thermocline. This setting instead favours establishment of atmospheric deep convection during strong warm anomalies of EP El Niño[8-11]; this triggers a nonlinear Bjerknes positive feedback, in which the response of zonal winds increases nonlinearly with positive SST anomalies, contributing to positive SST skewness[9,11,14].

The ENSO nonlinearity is depicted using the first two modes from Empirical Orthogonal Function (EOF) analysis[35] of monthly SST anomalies[8,10,13,17], each with a spatial pattern and a principal component (PC) time series (See Methods section 'Depiction of ENSO nonlinearity'). EP-ENSO is described by an E-index, defined as $(PC1-PC2)/\sqrt{2}$ (Ref. 8), and CP-ENSO by a C-index, defined as $(PC1+PC2)/\sqrt{2}$, such that the associated maximum warm anomaly is in the equatorial eastern and central Pacific, respectively. The relationship between the first two PCs is nonlinear[8], as measured by a quadratic relationship $PC2(t) = \alpha_D[PC1(t)]^2 + \beta_D PC1(t) + \gamma_D$ (Refs. 10, 13, 17). A greater dynamical nonlinearity coefficient $|\alpha_D|$ means stronger skewness in the E-index and C-index, therefore stronger nonlinearity of the ENSO system, and a clearer differentiation of the two ENSO regimes[17]. Here, we show that because ENSO is nonlinear, a tiny perturbation, akin to a flap of a butterfly wing[36], to an otherwise identical initial condition leads to a highly different ENSO evolution in the ensuing period, which in turn systematically modulates ENSO's response to greenhouse warming down the track.

Butterfly effect and ENSO across time

We examine such butterfly effects using 40 designated experiments of a fully coupled model (CESM-LE) (Ref. 25) (See Methods section 'Outputs of butterfly model experiments'), before assessing other large ensembles. The CESM-LE simulates a multi-member ensemble mean α_D of -0.37, with an inter-experiment range of -0.29 to -0.46 that encompasses the observed -0.31, and a reasonable ENSO variability pattern (**Fig. 1a**). This is associated with a reasonable simulation of the equatorial eastern Pacific cold tongue region where the nonlinear Bjerknes feedback operates[10,11,13,37], in turn ensuring a reasonable simulation of zonal advection, atmospheric thermal feedbacks, and less error compensation[37-41]. The butterfly experiments commence from 1920 under historical anthropogenic and natural forcings to 2005 and thereafter the Representative Concentration Pathway 8.5 (RCP8.5) future greenhouse-gas emission scenario[29] to 2099. An infinitesimally small random perturbation of the order of 10^{-14} °C in surface temperatures is added to an otherwise identical initial condition, possessing memory and inertia of the same internal variability. ENSO nonlinearity is characterised by the C-index and E-index obtained from an EOF analysis of quadratically detrended monthly SST anomalies over the whole 180 years (1920-2099). Removing the ensemble mean as a way of detrending makes virtually no difference to our result.

Under RCP8.5, there is little inter-experiment difference in global mean temperature or warming pattern featuring enhancement of the equatorial Pacific upper-ocean stratification that leads to an increased ocean-atmosphere coupling and increased E-index variability[17] (Extended Data Fig. 1, a-d). A total of 36 out of 40 experiments generate increased E-index variability (**Fig. 1b, c**). The multi-member ensemble increase is significant above the 99.9% confidence level, but vast inter-experiment differences exist.

To understand these differences, we examine ENSO statistics in the first 50 years (1920-1969). As the butterfly effect acts on the nonlinear system, ENSO SST variability over this initial period differs substantially from one experiment to another, as evident in the amplitude of E-index variability, and in frequency of strong El Niño and strong La Niña events, defined as E-index>1.5 s.d. and C-index<-1.5 s.d., respectively (**Fig. 1b, c, x-axis**). A higher E-index amplitude is associated with a higher frequency of strong El Niño, which is in turn conducive to strong La Niña[34], contributing to a greater C-index amplitude (Extended Data Fig. 2).

After the butterfly perturbation, what happens to ENSO is somewhat random. Owing to nonlinear dynamics, once an El Niño, La Niña, or a neutral state, occurs, it leads to a different subsequent evolution. An initial strong El Niño would favour a subsequent strong La Niña[7,9]; an initial neutral state, on the other hand, might persist, or be followed by an El Niño or La Niña; and an initial La Niña is likely to continue[7,9,10]. Thus, the different realisations of the first event lead to subsequent events that are never the same.

Strikingly, in experiments with initially stronger ENSO variability and a higher frequency of strong ENSO events, their amplitude and frequency in the future a century later are systematically smaller, and vice versa (**Fig. 1b, c**). Comparing the initial (1920-1969) and the last 50 (2050-2099) years, a total of 36 out of 40 experiments produce an increased E-index variability, but the increase ranges from a small percentage to 180%. ENSO rectification, in which a decadal period of high ENSO variability rectifies on the mean climate leading to an El Niño-like decadal state in turn promoting ENSO variability[42], would not explain the time scale or the systematic change. Below, we show that initial strong ENSO variability plants the seeds for its small future increase, through a cumulative heat loss to the atmosphere.

Cumulative heat loss due to nonlinearity

Atmospheric thermal damping is the dominant negative feedback on ENSO. The associated air-sea heat flux variability in the equatorial Pacific[6,16,37,39,43] is in turn dominated by ENSO, increasing with ENSO amplitude (Extended Data Fig. 2b, d) (see Methods section "Atmospheric thermal feedback and its nonlinearity"). Further, this damping is nonlinear[15,16] (Extended Data Fig. 3a, b). For example, in the equatorial eastern Pacific region, when El Niño warm SST anomalies establish atmospheric convection, increased cloud cover leads to reduced incoming shortwave radiation, damping the original warm anomalies; this represents an anomalous oceanic heat loss to the atmosphere, and is part of the El Niño discharge process[44]. Damping of La Niña cold anomalies is weaker than damping of El Niño warm anomalies, and represents an anomalous heat input into the ocean, as part of the La Niña recharge, but the associated heat flux is smaller because of a smaller amplitude of La Niña. The nonlinear damping can be represented as $NHF\,(t) = \alpha_T[E\text{-}index(t)]^2 + \beta_T\, E\text{-}index\,(t) + \gamma_T$, where *NHF(t)* is net heat flux positive into the ocean, and subscript T denotes "thermodynamical". The nonlinear coefficient α_T is negative. These properties are reproduced by the butterfly effect experiments (**Fig. 2a, b**).

Because of ENSO's nonlinear dynamics and thermodynamics, after several ENSO events, there is a net oceanic heat loss in the equatorial central and eastern Pacific. To illustrate this, we construct monthly *relative* surface flux field [*Rel-NHF(x, y, t)*] in all experiments referenced to the common monthly climatology averaged over the 70-year (1850-1919) period prior to the experiments, yielding 40 time-evolving *Rel-NHF(x, y, t)*. No detrending is carried out to avoid removing any trend induced by ENSO thermal damping. For example, accumulating the relative heat flux at a grid point on the equator (105^{o}W) over the initial 50 years shows a cumulative heat loss ranging from +334.3 to -2320.9 W m^{-2} over the 50 years, or 600 months across the 40 experiments (**Fig. 2c, y-axis**) (see also Extended Data Fig. 4). Experiments with greater initial ENSO variability systematically produce a greater cumulative heat loss, which can be represented by variability of detrended heat flux (**Fig. 2d**).

Modulation through ocean stratification

Accumulating the relative heat flux over the initial 50 years at grid-points yields 40 fields of cumulative heat fluxes. Regression of these fields onto inter-experiment E-index variability of the initial 50 years shows that experiments with stronger initial E-index variability systematically produce a greater cumulative oceanic heat loss in the equatorial central-to-eastern Pacific (**Fig. 2e**). Extension to the initial 100-year (1920-2019) period produces similar results (Extended Data Figs 4 and 5).

We average upper equatorial Pacific vertical temperatures across two groups of 10 experiments each, which produce top 10 highest and bottom 10 lowest values of initial E-index variability (blue star and orange diamond respectively, **Fig. 1a**) and calculate the trend over the first 50 (1920-1969), 100 (1920-2019), and 150 (1920-2070) years. Difference in the trend between the two groups (high variability minus low variability) over each period is mostly due to difference in cumulative heat flux associated with the difference in ENSO variability, because greenhouse warming-induced changes are removed by the subtraction. By the first 50 years, in experiments with greater initial ENSO variability, the greater cumulative oceanic heat loss in the equatorial Pacific leads to a greater heat discharge over the upper equatorial Pacific, initially maximum in the western Pacific, with a shallowed thermocline in the western but deepened thermocline in the eastern equatorial Pacific (**Fig. 3a**). Difference in other fields shows warmer surface equatorial eastern Pacific supported by weaker equatorial trade winds as a result of rectification by higher initial ENSO variability[42] (Extended Data Fig. 6). The rectified surface warming tends to facilitate atmospheric convection[45,46], maintaining initial high ENSO variability, which further increases the upper-ocean heat loss. The associated cooling subsequently spreads eastward (**Fig. 3b**), and eventually leads to cooling over much of the upper equatorial eastern Pacific by the end of 150 years (**Fig. 3c**), in an evolution analogous to the El Niño discharge process but on a long time scale. The associated upper-ocean cooling offsets greenhouse warming-induced upper-ocean warming and reduces enhancement in the associated upper-ocean stratification (Extended Data Fig. 1c), and the associated strengthening in ocean-atmosphere coupling. Thus, through its impact on the upper ocean, the ENSO system remembers its own past variability and modulates its future behaviour.

Robustness in other large ensembles

We examine two large ensembles with two other models, GFDL-CM3 with 20 experiments (Refs. 26, 27) and GFDL-ESM with 30 experiments (Refs. 27, 28), both simulating strong nonlinear dynamics and thermodynamics (Extended Data Fig. 7), and both under historical and RCP8.5 emission scenario (See Methods section "**Large ensembles with other models**"). For GFDL-CM3, an identical initial condition for all experiments is perturbed with a butterfly effect, as in CESM-LE, whereas for GFDL-ESM, the initial conditions are different. Under greenhouse warming, the majority of the experiments in GFDL-CM3 generate an increase in E-index variability, opposite to GFDL-ESM2M. Despite the contrasting response, in both models, experiments with smaller initial E-index variability systematically generate a greater increase (or a smaller reduction) in the future E-index variability (**Fig. 4a, b**). The results underscore the robustness of the self-modulating mechanism.

Self-modulation in an ensemble of models

We examine models participating in CMIP5 and CMIP6 forced by historical and RCP8.5 (or approximately equivalent SSP5-8.5) emission scenario[29,30] to 2099 (see Methods section "CMIP5 and CMIP6 models"). In this case, the initial condition, internal variability, and climate sensitivity are different across the models. The C-index and E-index for each model are obtained from EOF analysis on quadratically detrended monthly SST anomalies over the 200 years (1900-2099). Compared to the butterfly experiments, the dynamic and thermodynamic nonlinear coefficients $|\alpha_D|$ and $|\alpha_T|$ are generally smaller (Extended Data Fig. 7). We select 18 out of 34 CMIP5, and 9 out of 15 CMIP6 models that are presently available to us, based on their ability to simulate an $|\alpha_D|$ greater than 50% of the observed as in Ref. 17. These 27 models simulate an $\alpha_T < 0$ (Extended Data Fig. 7; Extended Data Fig. 3c, d). Overall, models with a stronger dynamical nonlinear coefficient also simulate a greater thermodynamical nonlinear coefficient[13,40]. As in the butterfly effect experiments, a greater E-index variability is systematically associated with a higher frequency of strong ENSO events, and stronger heat flux variability in the eastern Pacific (Extended Data Fig. 8).

A total of 22 out of the 27 (81%) models generate increased E-index variability. Importantly, models simulating greater ENSO variability in the initial 50-year period (1900-1949) systematically project a smaller increase in ENSO variability more than a century later (2050-2099), and vice versa (**Fig. 5a**). Greater E-index variability is associated with greater eastern Pacific heat flux variability (**Fig. 5b**), and the associated greater heat loss leads to a slower warming in the upper equatorial Pacific (**Fig. 5c**). The cooling offsets greenhouse warming-induced enhancement in upper-ocean stratification, leading to a smaller future increase in ENSO variability and in frequency of strong ENSO events (**Fig. 5d, e**). Difference in two groups of 10 models with top 10 highest and bottom 10 lowest values of initial ENSO variability shows greater variability and a greater E-index increase in the group with smaller initial variability (Extended Data Fig. 9), consistent with the butterfly effect experiments. Thus, despite the substantial differences among these models, the self-modulating ENSO response operates, underscoring its robustness. Increasing ensemble members does not alter our finding (Extended Data Fig. 10).

Conclusion and implications

Because the ENSO system is nonlinear, a butterfly perturbation leads to vastly different ensuing ENSO variations, which systematically modulate ENSO's response to greenhouse warming as much as a century later. The initial behaviour can be induced by decadal variability, stochastic forcing, or an infinitesimally small perturbation in initial conditions as seen in CMIP models. If stronger ENSO variability is promoted initially, ENSO nonlinear thermal damping causes a larger upper-oceanic heat loss to the atmosphere, which reduces greenhouse warming-induced enhancement in the equatorial Pacific upper-ocean stratification. This then decreases the associated strengthening in ocean-atmosphere coupling, reducing greenhouse warming-induced increases in ENSO variability at a later time. On the other hand, if ENSO variability is suppressed initially, stronger future ENSO variability ensues.

Our discovery of ENSO self-regulation offers a novel perspective for understanding ENSO in a changing climate, with important implications. The self-regulation increases the range of possibilities in the projected ENSO changes over the next century, because of past and future decadal variability in the system. In this context, the reported decrease in ENSO variability in recent decades[47-50] could potentially enhance the projected increase in ENSO variability (by ~35% from the current level, see Methods section "Impact of recent low ENSO variability"), which, though, could subsequently be reduced if there is higher-than-normal variability after 2020. Further, there is no deterministic equilibrium response of ENSO to greenhouse warming, because ENSO will continue to self-regulate in a non-stationary way around the equivalence of a chaotic "strange attractor" for a given level of greenhouse forcing. More broadly, ENSO is shaped by its own past and influences its own future, raising the possibility that the self-regulation mechanism operates on timescales transcending multidecadal and centennial, potentially contributing to ENSO variations as observed in the paleoclimate record.

Full methods and any associated references are available in the online version of the paper.

Additional information

Publisher's note: Springer Nature remains neutral with regard to jurisdictional claims in published maps and institutional affiliations.

References

1. Ropelewski, C. F. & Halpert, M. S. Global and regional scale precipitation patterns associated with the El Niño/Southern Oscillation. *Mon. Wea. Rev*. **115**, 1606-1626 (1987).
2. McPhaden, M. J., Zebiak, S. E. & Glantz, M. H. ENSO as an integrating concept in Earth science. *Science* **314**, 1740-1745 (2006).
3. Jonkman, S. N. Global Perspectives on Loss of human life caused by floods. *Natural Hazards* **34,** 151–175 (2005).
4. Kunii, O., Nakamura, S., Abdur, R. & Wakai, S. The impact on health and risk factors of the diarrhoea epidemics in the 1998 Bangladesh floods. *Public Health* **116,** 68–74 (2002).
5. del Ninno, C., & Dorosh, P. A. Averting a food crisis: private imports and public targeted distribution in Bangladesh after the 1998 flood. *Agricultural Economics* **25,** 337-346 (2001).
6. Cai, W., *et al*. More extreme swings of the South Pacific convergence zone due to greenhouse warming. *Nature* **488**, 365-369 (2012).
7. Frauen, C. & Dommenget, D. El Niño and La Niña amplitude asymmetry caused by atmospheric feedbacks. *Geophys. Res. Lett.* **37**, L18801 (2010).
8. Takahashi, K., Montecinos, A., Goubanova, K. & Dewitte, B. ENSO regimes: Reinterpreting the canonical and Modoki El Niño. *Geophys. Res. Lett.* **38**, L10704 (2011).
9. Choi, K.-Y., Vecchi, G. A. & Wittenberg, A. T. ENSO Transition, Duration, and Amplitude Asymmetries: Role of the Nonlinear Wind Stress Coupling in a Conceptual Model. *J. Climate* **26**, 9462-9476 (2013).
10. Dommenget, D., Bayr, T. & Frauen, C. Analysis of the non-linearity in the pattern and time evolution of El Niño Southern Oscillation. *Clim. Dyn.* **40**, 2825-2847 (2013).
11. Takahashi, K. & Dewitte, B. Strong and moderate nonlinear El Niño regimes. *Clim. Dyn.* **46**, 1627-1645 (2015).
12. Cai, W. *et al*. ENSO and Greenhouse warming. *Nature Clim. Change* **5**, 849-859. (2015).
13. Karamperidou, C., Jin, F.-F. & Conroy, J. L. The importance of ENSO nonlinearities in tropical Pacific response to external forcing. *Clim. Dyn*. **49**, 2695-2704 (2017).
14. Geng, T., Cai, W., Wu, L., & Yang, Y. Atmospheric convection dominates genesis of ENSO asymmetry. *Geophys. Res. Lett.*, **46**, 8387–8396 (2019).
15. Sun, D.-Z. *et al.* Radiative and dynamical feedbacks over the equatorial cold tongue: Results from nine atmospheric GCMs. *J. Climate* **19,** 4059–4074 (2006).
16. Lloyd, J., Guilyardi, E., Weller, H., & Slingo, J. The role of atmosphere feedbacks during ENSO in the CMIP3 models. *Atmos. Sci. Lett.,* **10**, 170–176 (2009).

17. Cai, W., *et al.* Increased variability of eastern Pacific El Niño under greenhouse warming. *Nature*, **564**, 201–206 (2018).
18. Wittenberg, A. T. Are historical records sufficient to constrain ENSO simulations? *Geophys. Res. Lett.* **36**, (2009).
19. Stevenson, S., Fox-Kemper, B., Jochum, M., Rajagopalan, B., & Yeager, S. G. ENSO model validation using wavelet probability analysis. *J. Climate* **23**, 5540-5547 (2010).
20. Stevenson, S. L. Significant changes to ENSO strength and impacts in the twenty - first century: Results from CMIP5. *Geophys. Res. Lett.* **39**, (2012).
21. Cobb, K. M., *et al*. Highly variable El Niño–Southern Oscillation throughout the Holocene. *Science*, **339**, 67-70 (2013).
22. Maher, N., Matei, D., Milinski, S., & Marotzke, J. ENSO change in climate projections: forced response or internal variability? *Geophys. Res. Lett.* **45**, 11-390 (2018).
23. Zheng, X. T., Hui, C., & Yeh, S. W. Response of ENSO amplitude to global warming in CESM large ensemble: uncertainty due to internal variability. *Clim. Dyn.* **50**, 4019-4035 (2018).
24. Lorenz, E. N. The predictability of a flow which possesses many scales of motion. *Tellus* **21**, 289-307, (1969).
25. Kay, J. E. *et al.* The community earth system model (CESM) large ensemble project : a community resource for studying climate change in the presence of internal climate variability. *Bull. Am. Meteorol. Soc.* **96**, 1333–1349 (2015).
26. Sun, L., Alexander, M. & Deser, C. Evolution of the global coupled climate response to Arctic sea ice loss during 1990–2090 and its contribution to climate change. *J. Climate* **31**, 7823–7843, (2018).
27. Deser, C. et al. Insights from Earth system model initial-condition large ensembles and future prospects. *Nature Clim. Change* **10**, 277–286 (2020)
28. Rodgers, K. B., Lin, J. & Frölicher, T. L. Emergence of multiple ocean ecosystem drivers in a large ensemble suite with an Earth system model. *Biogeosciences* **12**, 3301–3320 (2015).
29. Taylor, K. E., Stouffer, R. J. & Meehl, G. A. An overview of CMIP5 and the experiment design. *Bull. Amer. Meteor. Soc.* **93**, 485-498 (2012).
30. Eyring, V., Bony, S., Meehl, G. A., Senior, C. A., Stevens, B., Stouffer, R. J., and Taylor, K. E.: Overview of the Coupled Model Intercomparison Project Phase 6 (CMIP6) experimental design and organization, *Geosci. Model Dev.*, **9,** 1937-1958, (2016).
31. Cai, W., *et al*. Increasing frequency of extreme El Niño events due to greenhouse warming. *Nature Clim. Change* **4**, 111–116 (2014).
32. Kug, J.-S., Jin F.-F. & An S.-I. Two types of El Niño events: cold tongue El Niño and warm pool El Niño. *J. Clim.* **22**, 1499-1515 (2009).
33. Kao, H. Y. & Yu, J.-Y. Contrasting Eastern-Pacific and Central-Pacific Types of ENSO. *J. Clim.* **22**, 615-632 (2009).

34. Cai, W., *et al*. More frequent extreme La Niña events under greenhouse warming. *Nature Clim. Change* **5**, 132-137 (2015).
35. Lorenz, E. N. Empirical Orthogonal Functions and Statistical Weather Prediction. *Statistical Forecast Project Report 1* (MIT Department of Meteorology, 1956).
36. Lorenz, E. N. Deterministic nonperiodic flow. *J. Atmos. Sci.* **20,** 130-141 (1963).
37. Bayr, T., Dommenget, D., & Latif, M. Walker circulation controls ENSO atmospheric feedbacks in uncoupled and coupled climate model simulations. *Clim. Dyn.* 1-16 (2020).
38. Guilyardi, E., *et al*. Understanding El Niño in ocean–atmosphere general circulation models: Progress and challenges. *Bull. Amer. Meteor. Soc*. **90**, 325-340, (2009).
39. Bellenger, H., Guilyardi, É., Leloup, J., Lengaigne, M., & Vialard, J. ENSO representation in climate models: From CMIP3 to CMIP5. *Clim. Dyn.* **42**, 1999-2018, (2014).
40. Bayr, T., Latif, M., Dommenget, D., Wengel, C., Harlaß, J., & Park, W. Mean-state dependence of ENSO atmospheric feedbacks in climate models. *Clim. Dyn.* **50**, 3171-3194, (2018).
41. Bayr, T., Wengel, C., Latif, M., Dommenget, D., Lübbecke, J., & Park, W. Error compensation of ENSO atmospheric feedbacks in climate models and its influence on simulated ENSO dynamics. *Clim. Dyn.* **53**, 155-172, (2019).
42. Choi, J., An, S. I., Kug, J. S., & Yeh, S. W. The role of mean state on changes in El Niño's flavor. *Clim. Dyn*. **37**, 1205-1215 (2011).
43. Vijayeta, A., & Dommenget, D. An evaluation of ENSO dynamics in CMIP simulations in the framework of the recharge oscillator model. *Clim. Dyn.* **51**, 1753-1771, (2018).
44. Jin, F. F. An equatorial ocean recharge paradigm for ENSO. Part I: Conceptual model. *J. Atmos. Sci.* **54**, 811-829 (1997).
45. Zheng, X. T., Hui, C. & Yeh, S. W. Response of ENSO amplitude to global warming in CESM large ensemble: uncertainty due to internal variability. *Clim. Dyn.* **50**, 4019–4035 (2018).
46. Johnson, N. C. & Xie, S.-P. Changes in the sea surface temperature threshold for tropical convection. *Nature Geoscience* **3**, 842-845 (2010).
47. Hu, Z. Z., Kumar, A., Ren, H. L., Wang, H., L'Heureux, M., & Jin, F. F. Weakened interannual variability in the tropical Pacific Ocean since 2000. *J. Climate* **26**, 2601-2613, (2013).
48. Guan, C., & McPhaden, M. J. Ocean processes affecting the twenty-first-century shift in ENSO SST variability. *J. Climate* **29**(19), 6861-6879, (2016).
49. Hu, Z. Z., Kumar, A., Huang, B., Zhu, J., & Ren, H. L. Interdecadal variations of ENSO around 1999/2000. *J. Meteorol. Res.* **31**, 73-81, (2017).
50. Xu, K., Wang, W., Liu, B., & Zhu, C. Weakening of the El Niño amplitude since the late 1990s and its link to decadal change in the North Pacific climate. *Int. J. Climatol.* **39**, 4125-4138, (2019).

Acknowledgements

This work is supported by the Strategic Priority Research Program of Chinese Academy of Sciences, Grant No. XDB40000000. We acknowledge the World Climate Research Programme's Working Group on Coupled Modelling, which is responsible for CMIP, and we thank the climate modeling groups for producing and making available their model output. For CMIP the U.S. Department of Energy's Program for Climate Model Diagnosis and Intercomparison provides coordinating support and led development of software infrastructure in partnership with the Global Organization for Earth System Science Portals. We are grateful to various reanalysis groups for make the datasets available to us. PMEL contribution no. 5077. W.C., B.N., and A.S. are supported by CSHOR and the Earth System and Climate Change Hub of the Australian Government's National Environment Science Program. CSHOR is a joint research Centre for Southern Hemisphere Oceans Research between QNLM and CSIRO.

Author contributions

W.C. conceived the study and wrote the initial manuscript. B.N. performed analysis of butterfly experiments and T.G. carried out analysis of CMIP5 and CMIP6. All authors contributed to interpreting results, discussion of the associated dynamics, and improvement of this paper.

Competing interests

The authors declare no competing financial and non-financial interests.

Corresponding authors

Correspondence to Wenju Cai Wenju.Cai@csiro.au or Lixin Wu lxwu@ouc.edu.cn

Figure captions

Fig. 1 | Butterfly effect on ENSO variability. Shown are results from 40 experiments from the CESM-LE under historical (up to 2005) and thereafter representative concentration pathway 8.5 (RCP8.5) to 2099. Each experiment starts from identical initial condition in 1920 with small perturbation applied at a level of machine round-off error, which is referred to as the "bufferfly effect". **a,** SST standard deviation over the equatorial Pacific for the common 70-year period (1850-1919), showing typical SST variability pattern. **b, c,** The relationship of E-index standard deviation (s. d.), or strong ENSO frequency, at the initial 50-yr period (1920-1969) with their future change. The change is defined as the difference between last 50 years (2050-2099) and the initial 50 years, scaled for each member by the rate of global SST warming in each experiment. The butterfly effect results in different initial ENSO variability and the subsequent changes. In experiments with stronger initial ENSO variability, or higher frequency of strong ENSO events, their future increase is systematically smaller, supported by highly negative correlations significant above the 99% confidence level**.** Strong ENSO frequency in **c** is defined as the total number per 50 years of strong El Niño events (E-index > 1.5 s. d.) plus the total number of strong La Niña events (C-index < -1.5 s. d.) in the ENSO peak season of December-February. The blue stars and orange diamonds in **b** and **c** represent the 10 experiments with the weakest and strongest initial E-index variability, respectively. Correlation and p-value of a linear fit (red solid line) are also shown.

Fig. 2 | Impact on equatorial Pacific Ocean heat balance arising from butterfly effect. Shown is from a large ensemble with CESM-LE. **a, b,** Relationship between monthly E-index and monthly net heat flux over the eastern Pacific (5°S-5°N, 150°W-90°W), and between monthly C-index and monthly central Pacific (5°S-5°N, 160°E-90°W) net quadratically detrended heat flux into the ocean (W m^{-2}) for the initial 50 years (1920-1969) in CESM-LE. The red curve represents a nonlinear fit NHF $(t) = \alpha_T[E\text{-}index(t)]^2 + \beta_T\, E\text{-}index\, (t) + \gamma_T$, where $NHF(t)$ is net heat flux positive into the ocean, and subscript T denotes "thermodynamical". The nonlinear fit is statistically significant above the 99% confidence level. **c,** Inter-experiment relationship between E-index variability (1920-1969) and cumulative ocean heat loss (at equator 105^{o}W, indicated by black '+' in **e**). Before accumulation, monthly net heat flux fields referenced to the 70-year (1850-1919) common monthly climatology prior to butterfly effect are constructed. **d**, Inter-experiment relationship between heat flux variability (quadratically detrended) and the cumulative heat flux, showing a greater cumulative heat loss is associated with greater heat flux variability. The blue stars and orange diamonds in **c** and **d** represent the 10 experiments with the weakest and strongest initial E-index variability, respectively. Correlation and p-value of a linear fit (red solid line) are shown. **e,** Inter-experiment regression of 40 cumulative heat flux fields onto 40 values of E-index variability, both over the initial 50 years (1920-1969), showing an ENSO pattern of cumulative heat flux. In experiments in which the butterfly effect leads to greater initial ENSO variability, a greater cumulative ocean heat loss is generated along the equator. Statistical significance above **the 90%** and the 95% **confidence** level based on a two-tailed Student's *t*-test is indicated as **black stippling** and the green solid contour, respectively.

Fig. 3. | Self-modulating mechanism of ENSO response to greenhouse warming. a, Difference in linear trends of mean ocean temperature of the equatorial Pacific (average over 5°S-5°N) over the first 50 years (the 1920-1969 period) between average of the 10 experiments with strongest initial E-index variability (orange diamonds in **Fig. 1a**) and average of the 10 experiments with weakest initial E-index variability (blue stars in **Fig. 1a**). **b, c,** The same as **a** but for trends over the first 100 and 150 years, respectively. Statistical significance above **the 90%** and the 95% **confidence** level is indicated by **black stippling**

and the green solid contour, respectively. In experiments with greater initial ENSO variability, the greater cumulative oceanic heat loss in the equatorial Pacific leads to a slower warming over the upper equatorial Pacific by the end of the 50 years, with shallower thermocline in the west and deeper thermocline in the east (**a**), but subsequently cooling over the central-to-eastern (**b**), and eastern (**c**) equatorial Pacific, analogous to evolution of El Niño heat discharge but on a longer time scale. This process weakens greenhouse warming-induced stratification enhancement in the upper equatorial Pacific Ocean, leading to a smaller increase in ocean-atmosphere coupling. Consequently, in experiments with greater initial ENSO variability, the future increase in ENSO variability is weaker.

Fig. 4 | Robustness of ENSO self-modulation in large ensembles with other models. Shown is relationship between E-index standard deviation for the initial 50-years and its future change. The change is defined as the difference between last 50 years and the initial 50 years, scaled for each member by the rate of global SST warming in each experiment. **a**, GFDL-CM3, which has 20 members commencing from 1920. The initial 50-years is 1920-1969 and last 50-years is 2050-2099. Each member starts from an otherwise identical initial condition except a butterfly perturbation to the atmosphere component, generating the initial ensemble spread. **b,** GFDL-ESM2M, which has 30 members commencing from 1950. The initial 50-years is 1950-1999 and the last 50-years is 2050-2099. Each member commences from a different initial coupled model state taken as the snapshot at the end of 30 days in January 1950, respectively. Correlation and p-value of a linear fit (red solid line) are also shown.

Fig. 5. | Self-modulating mechanism of ENSO response in CMIP5 and CMIP6 models. Shown are 27 models, i.e., 18 out of 34 CMIP5 models and 9 out of 15 CMIP6 models that produce a dynamic nonlinear coefficient α_D <-0.155 (i.e. 50% of the observed amplitude[17], and thermodynamic nonlinear coefficient α_T <0. **a**, Inter-model relationship between initial 50-year (1900-1949) E-index variability and its future change (2050-2099 minus 1900-1949). As in the butterfly effect experiments, a greater initial E-index variability leads to a smaller future increase in E-index variability. **b**, Inter-model relationship showing greater initial 50-year (1900-1949) E-index variability is associated with greater initial heat flux (5^oN-5^oS, 150^oW-90^oW), a surrogate of cumulative ocean heat loss. **c**, Inter-model regression of mean equatorial (average over 5^oS-5^oN) upper-ocean temperature change (2050-2099 minus 1900-1949) onto the initial 50 years (1900-1949) heat flux variability. Future changes are scaled by the corresponding global-mean SST warming in each model. Black stippling and green solid contours indicate statistical significance above the 90% and 95% confidence level, respectively, based on a two-tailed Student's *t*-test. Greater initial variability in ENSO and the associated greater heat loss contributes to a weaker upper equatorial Pacific Ocean warming. **d**, **e,** Inter-model relationship showing a greater initial (1900-1949) cumulative heat loss as indicated by greater heat flux variability leads to a smaller future increase (2050-2099

minus 1900-1949) in E-index variability and in frequency of strong ENSO events. Strong ENSO frequency in **e** is defined as the total number per 50 years of strong El Niño events (E-index > 1.5 s.d.) plus the total number of strong La Niña events (C-index < -1.5 s.d.) in the ENSO peak season of December-February. Correlation and p-value of a linear fit (red solid line) in scatter plots **a, b, d, e** are also shown.

METHODS

Depiction of ENSO nonlinearity. To depict ENSO nonlinearity, at least two indices are needed and this can be obtained from a combination of the first two modes from Empirical Orthogonal Function (EOF) (Ref. 35) analysis of monthly SST anomalies[8,10,13,17], in an equatorial domain (15°S–15°N, 140°E–80°W). Each mode is described by a spatial pattern and a principal component (PC) time series that is scaled to have a variance of unity. The first principal mode captures the classical El Niño pattern, while the second mode depicts anomalous east-minus-west SST anomalies across the equatorial Pacific, anomalously warm in the central Pacific but cold in the eastern Pacific. ENSO is reflected by a nonlinear relationship between the first two PCs, which is measured by a quadratic relationship[8,10,13,17] $PC2(t) = \alpha_D[PC1(t)]^2 + \beta_D PC1(t) + \gamma_D$ (Subscript D indicates "dynamical"). A greater $|\alpha_D|$ means a higher level of nonlinearity, stronger skewness in the E-index and C-index, and therefore stronger nonlinearity of the ENSO system, and clearer differentiation of the two types of ENSO events[17]. For the observed, the value of α_D is -0.31 (Ref. 17). The E-index is defined as $(PC1\text{-}PC2)/\sqrt{2}$ (Ref. 8), such that the associated maximum warm anomaly is in the equatorial eastern Pacific. The C-index is defined as $(PC1+PC2)/\sqrt{2}$, such that the associated maximum cold anomaly is in the equatorial central Pacific. The two indices describe EP- and CP-ENSO regimes, each associated with a suite of distinct processes that lead to the positive and negative skewness in the E-index and C-index, respectively, as discussed in main text.

Butterfly effect experiments. We take 40 members of simulation experiments using a climate model (CESM-LE) to examine the impact of internal variability. These experiments are identically subject to greenhouse warming which follow the CMIP5 design protocol[25] with historical emissions of greenhouse gases applied from 1850/1920 to 2005 and RCP8.5 forcing from 2006 to 2100. Ensemble member 1 was carried out from 1850, then the other members are created from perturbations of ensemble member 1 in 1920. The initial condition is identical (end of 1919), except with an imposed infinitesimally small random perturbation to the atmospheric state at machine level round-off error[25] (10^{-14} °C in surface temperature) at the beginning of 1920 that represents small perturbation equivalent to the flap of a butterfly wing. Therefore, these experiments possess the same memory and inertia of initial internal variability. Each member then evolves freely, and is subject to stochastic processes, thus any ensuing difference between model experiment members is due to internal variability.

CP- and EP-ENSO in these experiments are characterized by C-index and E-index, respectively, as in the observed. Overall, the model simulates a reasonable level of nonlinear properties of ENSO, with a multi-member ensemble mean α_D of -0.37, compared with an observed value of -0.31 (Extended Data Fig. 7).

Atmospheric thermal feedback and its nonlinearity. Atmospheric heat flux into the equatorial ocean plays an important role in the ENSO cycle and usually represents a negative feedback, dominated by shortwave and latent heat flux feedbacks[15,16]. The shortwave component can be highly nonlinear but underestimated in most climate models, mainly associated with a cold equatorial mean SST bias and is better represented in models with a realistic mean state of the rising branch of the Walker Circulation[16,39,40] (Extended Data Fig. 7). During an El Niño, a warmer SST leads to an increase in atmospheric convection, high clouds, and a decrease in surface shortwave heat flux; this feedback is negative. During La Niña, while the opposite is generally true but tends to be weaker, because a cold SST anomaly may also stabilise the atmospheric boundary layer and promote the formation of stratiform boundary layer clouds[51,52], decreasing shortwave heat flux at the surface. Thus, the atmospheric thermal feedback damps warm SST anomalies but the damping weakens for cold SST anomalies. We describe the level of nonlinearity in atmospheric thermal damping by the quadratic relationship $NHF(t) = \alpha_{tT}[E\text{-}index(t)]^2 + \beta_T\, E\text{-}index(t) + \gamma_T$, where subscript T denotes "thermodynamical" representing thermal damping, and $NHF(t)$ is the net heat flux at a grid-point, positive into the ocean. Because the damping increases with ENSO amplitude, net heat flux variability increases with ENSO variability. In conjunction with ENSO nonlinearity, that is, greater El Niño amplitude than La Niña amplitude, the thermal feedback leads to a net heat loss to the atmosphere. This depiction of nonlinear damping was applied to re-analysis datasets and outputs from coupled global climate models.

We construct time series of net heat flux anomalies over the eastern equatorial Pacific, referenced to the first-100 and first 70-year climatology, for CMIP models and butterfly effect experiments, respectively. As done for ENSO SST, we quadratically detrend the time series over the full period and normalise the time series with the standard deviation over the *full* period. Variability of the first 50 years or last 50 years for each model or experiment is then calculated from the normalised time series. An exception is cumulative heat flux shown in **Fig. 2b, c**, which shows raw data cumulative over the first 50 years without detrending of heat flux *relative* to monthly climatology averaged over the previous 70 years (common period for all experiments) to give readers a gauge of the real amplitude.

To diagnose the observed thermodynamic nonlinearity, we use three SST reanalysis products and two atmospheric reanalyses. We focus on the 1979-2017 period, which is common to all datasets, and data quality is high. These reanalyses include: Five ensemble members of ORA-s5 (ECMWF Ocean Analysis System: ORA-s5)[53] containing both SST and surface heat flux fields; HadISST v1.1 (Hadley Centre Sea Ice and Sea Surface Temperature dataset version 1.1)[54]; ERSST v5 (Extended Reconstructed Sea Surface Temperature version 5)[55]; NCEP/NCAR reanalysis (the National Center for Environmental Prediction and the National Center for Atmospheric Research global reanalysis)[56] and ERA5 (ECMWF the fifth major global reanalysis)[57]. Monthly detrended anomalies are constructed with reference to the mean climatology over the full period. EOF analysis on monthly SST anomalies are conducted to obtain E-index and C-index. Heat flux averages over the equatorial central Pacific (5°S-5°N, 160°E-150°W) and eastern Pacific (5°N-5°S, 150°W-90°W) are obtained and the relationship is shown in Extended Data Fig. 3.

Large ensembles with other models. We examine another two sets of large ensembles with two different fully coupled models under historical and RCP8.5 emission scenario. These are GFDL-CM3 (Refs. 26, 27) and GFDL-ESM2M (Refs. 27, 28), both simulating strong nonlinear ENSO dynamics and thermodynamics (See Extended Data Fig. 7). There are 20 experiments with GFDL-CM3 commencing from 1920, and 30 experiments with GFDL-ESM2M commencing from 1950 all under historical and RCP8.5 emission scenario[27]. For the GFDL-CM3, all 20 members begin from a single coupled model state, with a butterfly perturbation introduced in the atmospheric component, as in CESM-LE. For GFDL-ESM2M, the initial conditions for the 30 ensemble members for 1 January 1950 differ in the state of the atmosphere/land/ocean/sea ice components of the Earth system model, accomplished by using a model state snapshot at the end of days 1–29 in January 1950 as the initial model states for 1 January 1950 for each of the ensemble members 2–30, respectively (Ref. 28).

CMIP5 and CMIP6 models. The EOF approach was applied to reanalysis datasets, and outputs from CMIP5 forced by historical forcing up to 2005 and RCP8.5, and CMIP6 forced by historical forcing up to 2014 and thereafter approximately equivalent to RCP8.5 (or Shared Socioeconomic Pathway-5-8.5) emission scenario to 2099 (Refs. 29, 30), covering a period of transient CO_2 increase into 2099. Monthly anomalies referenced to the climatology of the first 100 years were constructed and quadratically detrended. We select 27 CMIP5 and CMIP6 models that can simulate ENSO nonlinearity as measured by α_D. One experiment (the first simulation) from each model is used, covering the period 1900–2099. We compare results in a group of models with an $|\alpha_D|$ greater than at least half of the observed, as in Ref. 17. These models simulate the nonlinear atmospheric thermal feedback with an α_T that is negative and all models but one produce an α_T greater than 50% of the observed amplitude (see Extended Data Fig. 7**).** Increasing ensemble members does not alter our finding (Extended Data Fig. 10).

Impact of recent low ENSO variability. Based on a reanalysis[54], observed E-index variability over the 2000-2019 period is at 0.87 s.d., that is 0.13 s.d. lower than the average over the 120 years since 1900, set at 1.0 s.d.. To assess the impact of the current low level of

E-index variability, we examine the inter-model relationship across the 27 selected models between the current (2000-2019) and future (2050-2099) E-index variability, and obtain a sensitivity of ~0.55 s.d. increase in future E-index per 1.0 s.d. decrease in the current E-index, which is statistically significant above the 99% confidence level. The multi-model ensemble average increase in E-index variability over the two periods is 0.19 s.d.. Using the sensitivity and the enormous decrease in current E-index variability of 0.13 s.d., we estimate that the recent low E-index variability has the potential to increase future E-index variability by ~37% (that is, 0.13 x 0.55 / 0.19), everything else being equal. By the same mechanism, any increase in variability after 2020 will have an opposing effect on the projected change.

Data availability. Data related to the paper can be downloaded from the following:

- ORA-s5, https://www.ecmwf.int/en/research/climate-reanalysis/ocean-reanalysis;
- HadISST v1.1, https://www.metoffice.gov.uk/hadobs/hadisst/;
- ERSST v5, https://www.ncdc.noaa.gov/data-access/marineocean-data/extended-reconstructed-sea-surface-temperature-ersst-v5/;
- NCEP/NCAR reanalysis, https://www.esrl.noaa.gov/psd/data/gridded/data.ncep.reanalysis.derived.surfaceflux.html/;
- ERA5, https://www.ecmwf.int/en/forecasts/datasets/reanalysis-datasets/era5;
- CMIP5, https://esgf-node.llnl.gov/projects/cmip5/;
- CMIP6, https://esgf-node.llnl.gov/projects/cmip6/;
- CESM-LENS, http://www.cesm.ucar.edu/projects/community-projects/LENS/data-sets.html

Code availability. Codes for calculating EOF, the parameter $|\alpha_D|$ can be downloaded from: https://drive.google.com/open?id=1d2R8wKpFNW-vMIfoJsbqIGPIBd9Z_8rj. All codes are available upon request.

Methods References

51. Philander, S. et al. Why the ITCZ is mostly north of the equator. *J. Climate,* **9,** 2958–2972 (2006).
52. Xie, S.-P. The shape of continents, air-sea interaction, and the rising branch of the Hadley circulation. The Hadley Circulation: Present, Past and Future, H. F. Diaz and R. S. Bradley, Eds., Advances in Global Change Research, Vol. 21, Kluwer Academic Publishers, 121–152 (2005).
53. Zuo, H., Balmaseda, M. A., & Mogensen, K. The new eddy-permitting ORAP5 ocean reanalysis: description, evaluation and uncertainties in climate signals. *Climate Dynamics*, **49,** 791-811(2017).

54. Rayner, N. A. et al. Global analyses of sea surface temperature, sea ice, and night marine air temperature since the late nineteenth century. *J. Geophys. Res.* **108**, 4407 (2003).
55. Huang, B. et al. Extended reconstructed sea surface temperature version 5 (ERSSTv5), upgrades, validations, and intercomparisons. *J. Clim.* **30**, 8179– 8205 (2017).
56. Kalnay, E. et al. The NCEP/NCAR 40-year reanalysis project. *Bull. Am. Meteorol. Soc.* **77,** 437–472 (1996).
57. Hersbach, H. & Dee, D. "ERA-5 reanalysis is in production", ECMWF newsletter, number 147, Spring 2016, p. 7 (2016).

Captions for Extended Data

Extended Data Fig. 1 | Ensemble averaged warming and ENSO change in the butterfly effect experiments. Shown are from 40 butterfly effect experiments of CESM-LE. **a**, Time series of global mean sea surface temperature (SST). The red curve represents the ensemble mean. **b**, Multi-experiment ensemble mean SST and wind stress difference between the last 50-year (2050-2099) and the initial 50-year (1920-1969) periods. **c**, Same as in **b** but for ocean temperature along the Equator averaged between 5°S-5°N, showing an intensification of stratification along the equatorial upper ocean as in Ref. 17, enhancing the ocean-atmosphere coupling. **d,** E-index variability in the initial 50-year period (blue bars) and the last 50-year period (red bars) for each experiment and the multi-experiment ensemble mean. The error bars represent one standard deviation value of inter-experiment E-index variability for the two periods, respectively.

Extended Data Fig. 2 | ENSO properties in initial and future climate in the butterfly effect experiments. Shown are from 40 butterfly effect experiments of CESM-LE. **a,** Inter-experiment relationship between E-index and C-index standard deviation (s. d.) for the initial 50-year (1920-1969) period. **b,** As in **a,** inter-experiment relationship between E-index variability and variability of eastern Pacific (EP, 5°S-5°N, 150°W-90°W) net heat flux (s. d.). **c, d,** The same as **a, b,** respectively but for the future 50-year (2050-2099) period. The blue stars and orange diamonds represent the 10 experiments with the weakest and strongest initial E-index variability, respectively. Experiments with a greater E-index variability systematically produce greater heat flux variability, and greater C-index variability as strong El Niño events lead to strong La Niña events. These properties are seen in both initial and future climate. Statistics (i.e. correlation and p-value) of a linear fit (red solid line) are shown. The relationship is statistically significant above the 99% confidence level.

Extended Data Fig. 3 | Nonlinear thermal damping aggregated over observational datasets and over 27 selected CMIP5 and CMIP6 models. a, Observed monthly E-index vs normalized monthly surface net heat flux anomalies over the eastern Pacific (EP, 5°S-5°N, 150°W-90°W) for the period of 1979-2017. **b,** As in **a**, but for observed monthly C-index vs normalized monthly surface net heat flux anomalies over the central Pacific (CP, 5°S-5°N, 160°E-150°W). Also shown are the quadratic fit (red solid line), for example, with E-index, in terms of $NHF\ (t) = \alpha_T\ [E\text{-}index(t)]^2 + \beta_T\ E\text{-}index\ (t) + \gamma_T$, and corresponding thermodynamic nonlinear coefficient "α_T" associated with EP and CP ENSO. Three SST reanalysis products and two atmospheric reanalyses[53-57] are used here (see Methods "Atmosphere thermal feedback and its nonlinearity"). **c, d,** As in **a, b,** respectively, but for 27 selected CMIP5 and CMIP6 models (see Extended Data Fig. 7).

Extended Data Fig. 4 | ENSO thermal damping and cumulative ocean heat flux in the butterfly effect experiments. Shown are from 40 butterfly effect experiments of CESM-LE. Illustration is given in **a, b,** time series E-index (black) and net heat flux (red) in the eastern Pacific (at equator 105°W) in experiments with strongest (Run 14) and weakest (Run 24) E-index variability in the initial (1920-1969) 50 years. **c**, Eastern Pacific cumulative net heat flux for the two experiments. Raw monthly net heat flux fields referenced to the 70-year (1850-1919) common monthly climatology prior to butterfly effect is constructed first before accumulation. Greater cumulative heat loss by 1969 (end of the initial 50 years, indicated by the vertical black line) is generated due to greater initial ENSO variability, reducing upper ocean warming due to greenhouse effect.

Extended Data Fig. 5 | ENSO thermal damping in the initial 100 years after the butterfly effect. Shown are from 40 butterfly effect experiments of CESM-LE. **a, b,** Relationship between monthly E-index and monthly net heat flux over the eastern Pacific (EP, 5°S-5°N, 150°W-90°W), and between monthly C-index and monthly central Pacific (CP, 5°S-5°N, 160°E-90°W) quadratically detrended net heat flux into ocean (W m^{-2}) for the initial 100 years (1920-2019). Thermal damping takes heat out of the ocean during El Niño and puts heat into the ocean during La Niña, but because El Niño is greater in amplitude, after several ENSO events, net heat is taken out of the ocean. **c,** Inter-experiment relationship showing that greater initial ENSO variability, hence a greater amount of cumulative ocean heat loss (at equator 105°W, indicated by black '+' in **e,** positive out of ocean) is generated. Raw monthly net heat flux fields referenced to the 70-year (1850-1919) common monthly climatology prior to butterfly effect is constructed first before accumulation. The cumulative oceanic heat loss can be surrogated by heat flux variability, as seen in **d**, showing a greater cumulative heat loss is associated with greater heat flux variability. The blue stars and orange diamonds in **c** and **d** represent the 10 experiments with the weakest and strongest initial E-index variability, respectively. Correlation and p-value of a linear fit (red solid line) are shown. **e,** Inter-experiment regression of 40 cumulative heat flux fields onto 40 values of E-index variability, both over the initial 100 years (1920-2019), showing an ENSO pattern of cumulative heat flux. In experiments in which the butterfly effect leads to greater initial ENSO variability, a greater cumulative ocean heat loss is generated along the equator.

Statistically significance above **the 90%** and the 95% confidence level based on a two-tailed Student's *t*-test is indicated as **black stippling** and the green solid contour, respectively.

Extended Data Fig. 6 | Difference between two groups of experiments with strong and weak initial E-index variability. Shown are from 40 butterfly effect experiments of CESM-LE. The difference indicates the impact due to different ENSO variability between the two groups. **a**, SST (°C) and wind stress (N m^{-2}) difference between the 10 experiments with the strongest E-index variability in the initial 50-year period (1920-1969) and the 10 experiments with the weakest E-index variability for the same period (See Main Fig. 1a, orange diamonds and blue stars, respectively). **b**, Same as in **a** but for the upper 150m ocean temperature (°C). Stippling indicates where the difference between the two ensembles is significant above the 90% confidence level, based on a two-tailed Student's *t*-test and the green solid contour represents the 95% confidence level.

Extended Data Fig. 7 | Selection of CMIP5 and CMIP6 models. Shown are 27 models, that is, 18 out of 34 CMIP5 models and 9 out of 15 CMIP6 models that produce both dynamic nonlinear coefficient α_D <-0.155, that is, greater than half of the observed amplitude[17] and these also produce a thermodynamic nonlinear coefficient α_T <0 with all but one simulating half of the observed based. In general, a greater α_T is associated with a greater α_D with a correlation coefficient of 0.47 using all models. Selected models are marked by symbols filling in different colors, while non-selected models are indicated with black and gray without filling. Each ensemble member and the multimember ensemble mean for CESM-LE are shown in filled blue and red circle, respectively.

Extended Data Fig. 8 | ENSO properties in CMIP5 and CMIP6 models. a, b, Inter-model relationship of E-index variability with strong ENSO frequency and with eastern Pacific (5°S-5°N, 150°W-90°W) heat flux variability, receptively, for the initial 50-year period (1900-1949). **c, d,** The same as **a, b,** respectively, but for the last 50-year period (2050-2099). Models with a higher E-index variability systematically generate a higher frequency of strong ENSO events and a stronger heat flux variability. Shown are 27 models, i.e., 18 out of 34 CMIP5 models and 9 out of 15 CMIP6 models that produce both a dynamic nonlinear coefficient α_D< -0.155, i.e. greater than half of the observed amplitude[17] and a thermodynamic nonlinear coefficient α_T <0. Strong ENSO frequency in **a, c** is defined as the total number per 50 years of strong El Niño events (E-index > 1.5 s.d.) plus the total number of strong La Niña events (C-index < -1.5 s.d.) in ENSO peak season of December-February. Correlation and p-value of a linear fit (red solid line) are shown. In all scatter plots, the relationship is statistically significant above the 99% confidence level.

Extended Data Fig. 9 | Evolution of ENSO variability in CMIP5 and CMIP6 models. a, Inter-model relationship between the last (2050-2099) and initial (1900-1949) 50-year period in E-index variability, showing an inverse relationship statistically significant above the 99%

confidence level, that is, models that generate a greater variability in the initial period systematically produce a smaller future variability. Shown are 27 models, that is, 18 out of 34 CMIP5 models and 9 out of 15 CMIP6 models that produce both a dynamic nonlinear coefficient α_D <-0.155 (greater than half of the observed amplitude[17]) and a thermodynamic nonlinear coefficient α_T <0. **b,** Evolution of E-index variability, measured by a 50-year running window, moving forward every year from 1900 and recorded at the initial year, for 10 models with strong initial E-index variability (red box in **a**) and 10 models with weak initial E-index variability (blue box in **a**). Solid red (blue) lines and red (blue) shadings indicate multi-model average and inter-model spread (one standard deviation value), respectively, of the 10 models with strong (weak) initial E-index variability. ENSO variability in models with weaker initial variability exhibits a faster increase in response to greenhouse warming during the ensuing periods, with a final amplitude that exceeds that in models with stronger initial ENSO variability. Different running window lengths (for example, 40-year, 60-year) and different sample sizes of model groups for averaging (for instance 7 or 13 models with largest initial E-index variability versus 7 or 13 models with smallest initial E-index variability, respectively) produce qualitatively similar behavior.

Extended Data Fig. 10 | Initial ENSO variability and its future change in all available runs of CMIP5 and CMIP6 models. Shown are the 27 selected models, that is, 18 out of 34 CMIP5 models and 9 out of 15 CMIP6 models that produce both a dynamic nonlinear coefficient α_D <-0.155 (greater than half of the observed amplitude[17]) and a thermodynamic nonlinear coefficient α_T <0. **a**, Inter-model relationship between initial 50-year (1900-1949) E-index variability and its future change (2050-2099 minus 1900-1949) scaled by the corresponding global-mean SST warming in each model. **b,** As in **a,** but for C-index. Run numbers are indicated next to the model names (for example, r1, r2 and so on).

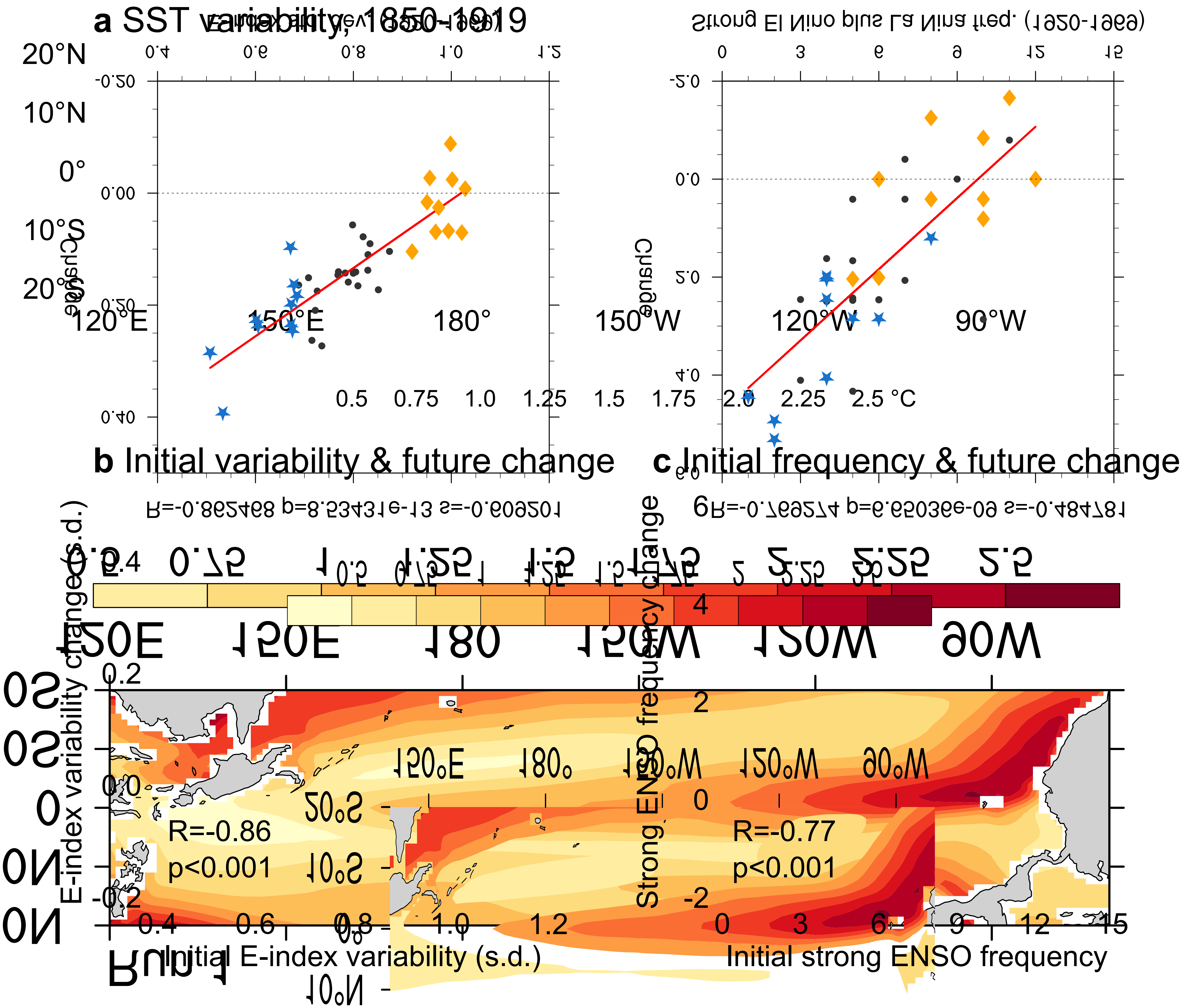
a SST variability, 1850-1919
20°N
10°N
0°
10°S
20°S
120°E
150°E
180°
150°W
120°W
90°W
0.5
0.75
1.0
1.25
1.5
1.75
2.0
2.25
2.5 °C
b Initial variability & future change
c Initial frequency & future change
E-index variability change (s.d.)
0.2
0.0
-0.2
0.4
0.6
0.8
1.0
1.2
R=-0.86
p<0.001
Initial E-index variability (s.d.)
Strong ENSO frequency change
4
2
0
-2
0
3
6
9
12
15
R=-0.77
p<0.001
Initial strong ENSO frequency

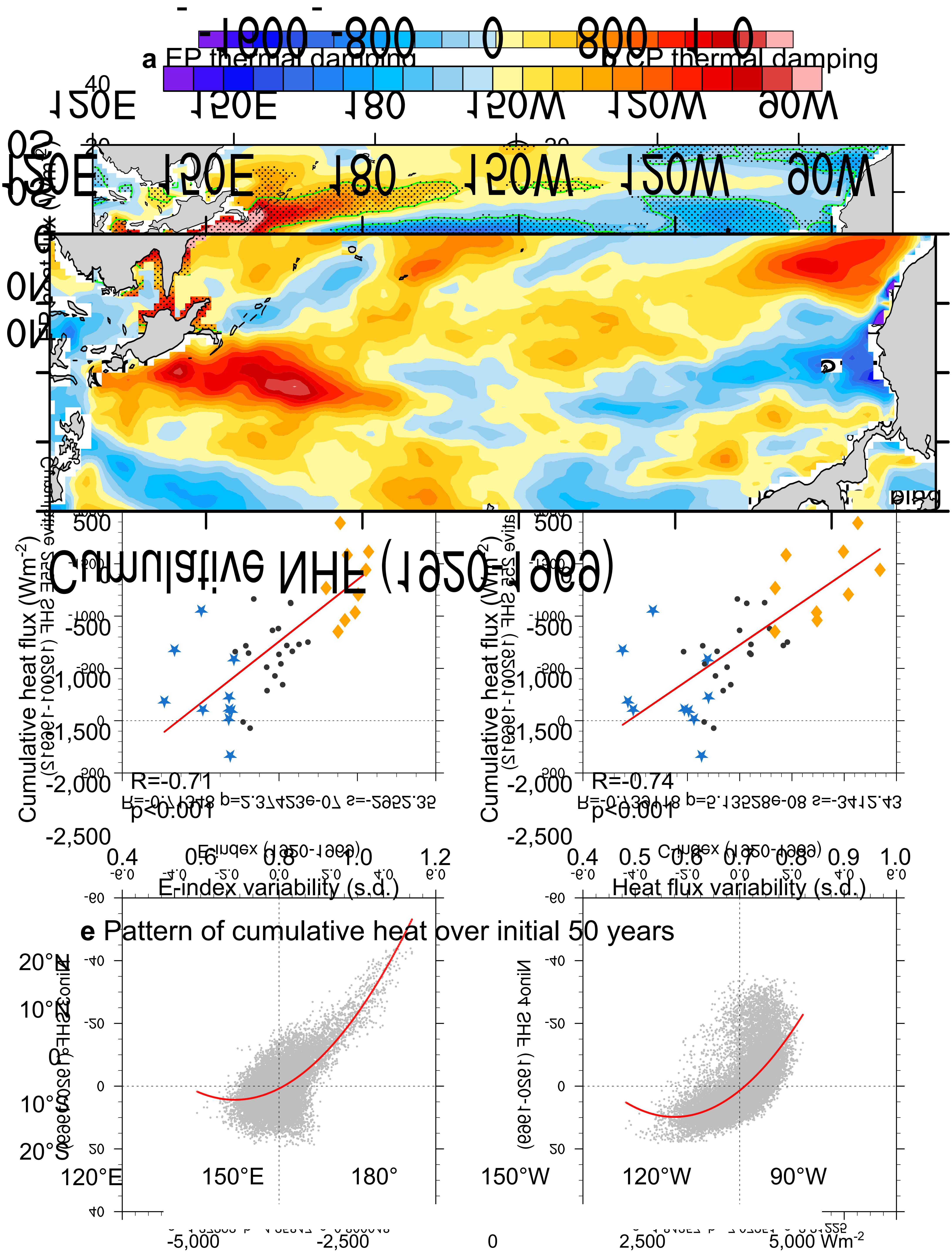
a EP thermal damping
b CP thermal damping
Cumulative heat flux (Wm-2)
R=-0.71
p<0.001
R=-0.74
p<0.001
E-index variability (s.d.)
Heat flux variability (s.d.)
e Pattern of cumulative heat over initial 50 years
20°N
10°N
0°
10°S
20°S
120°E
150°E
180°
150°W
120°W
90°W
-5,000
-2,500
0
2,500
5,000 Wm-2

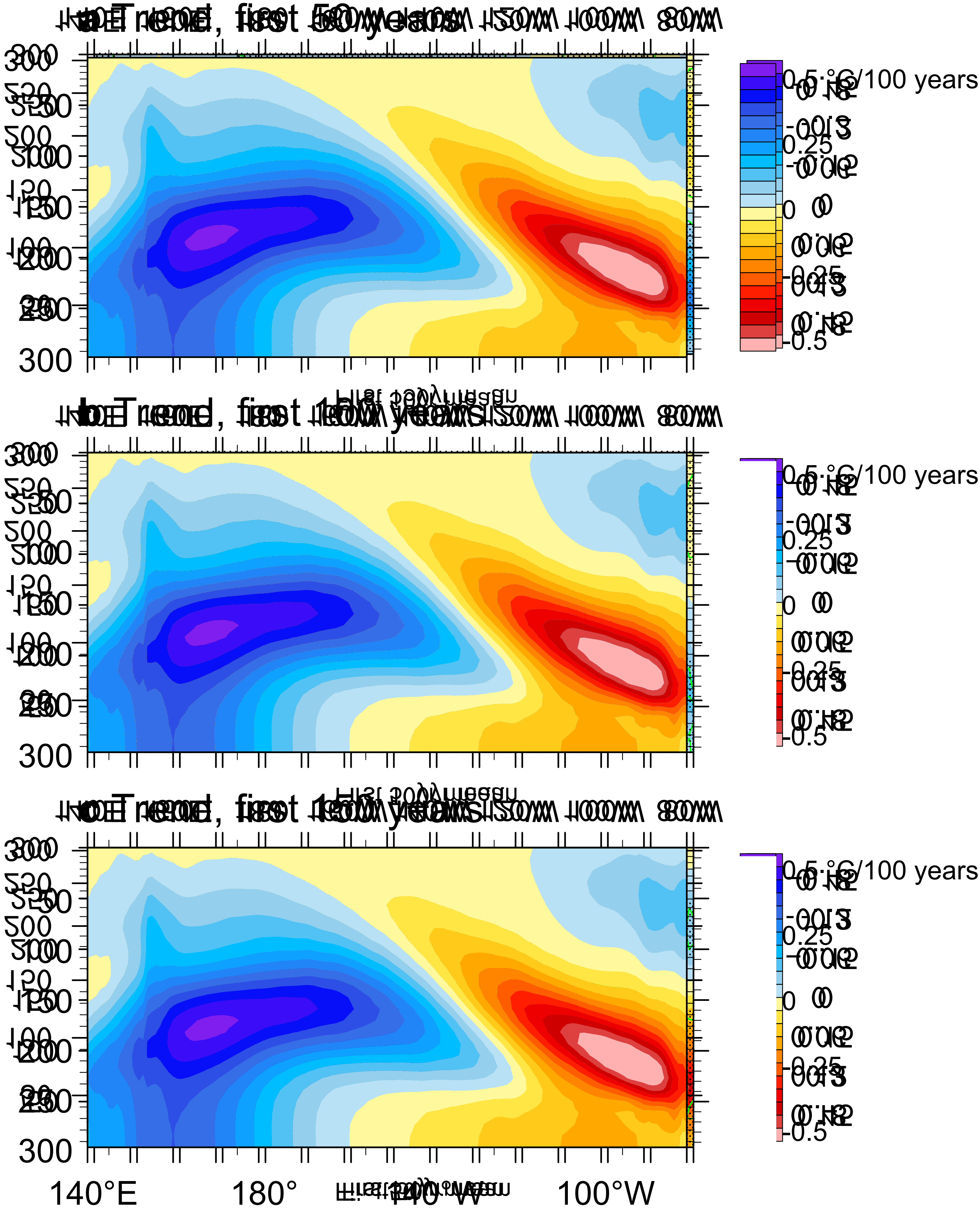

°C/100 years
140°E
180°
100°W

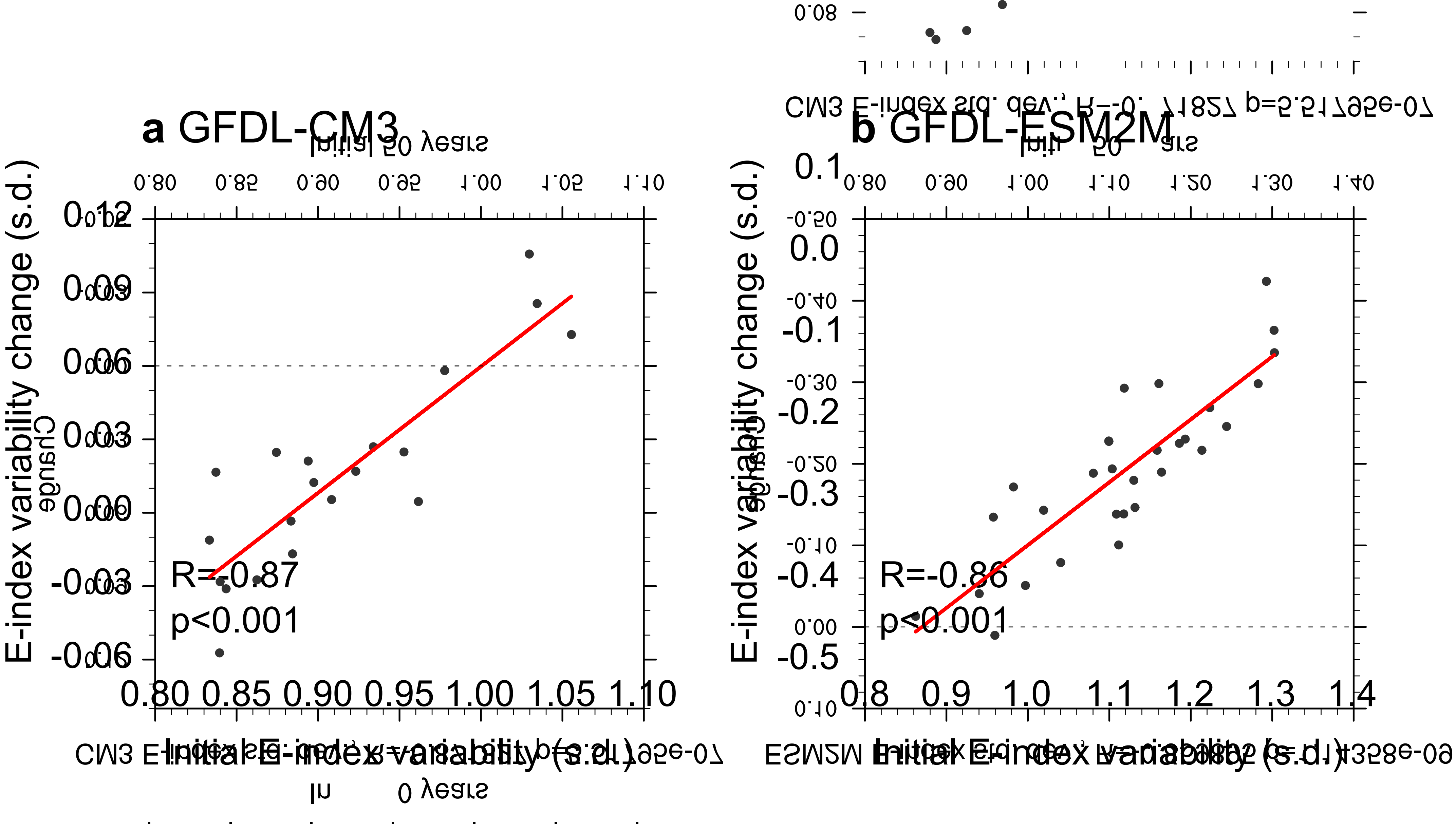
a GFDL-CM3
b GFDL-ESM2M
E-index variability change (s.d.)
Initial E-index variability (s.d.)
R=-0.87
p<0.001
R=-0.86
p<0.001
0.80 0.85 0.90 0.95 1.00 1.05 1.10
0.8 0.9 1.0 1.1 1.2 1.3 1.4
0.12 0.09 0.06 0.03 0.00 -0.03 -0.06
0.1 0.0 -0.1 -0.2 -0.3 -0.4 -0.5

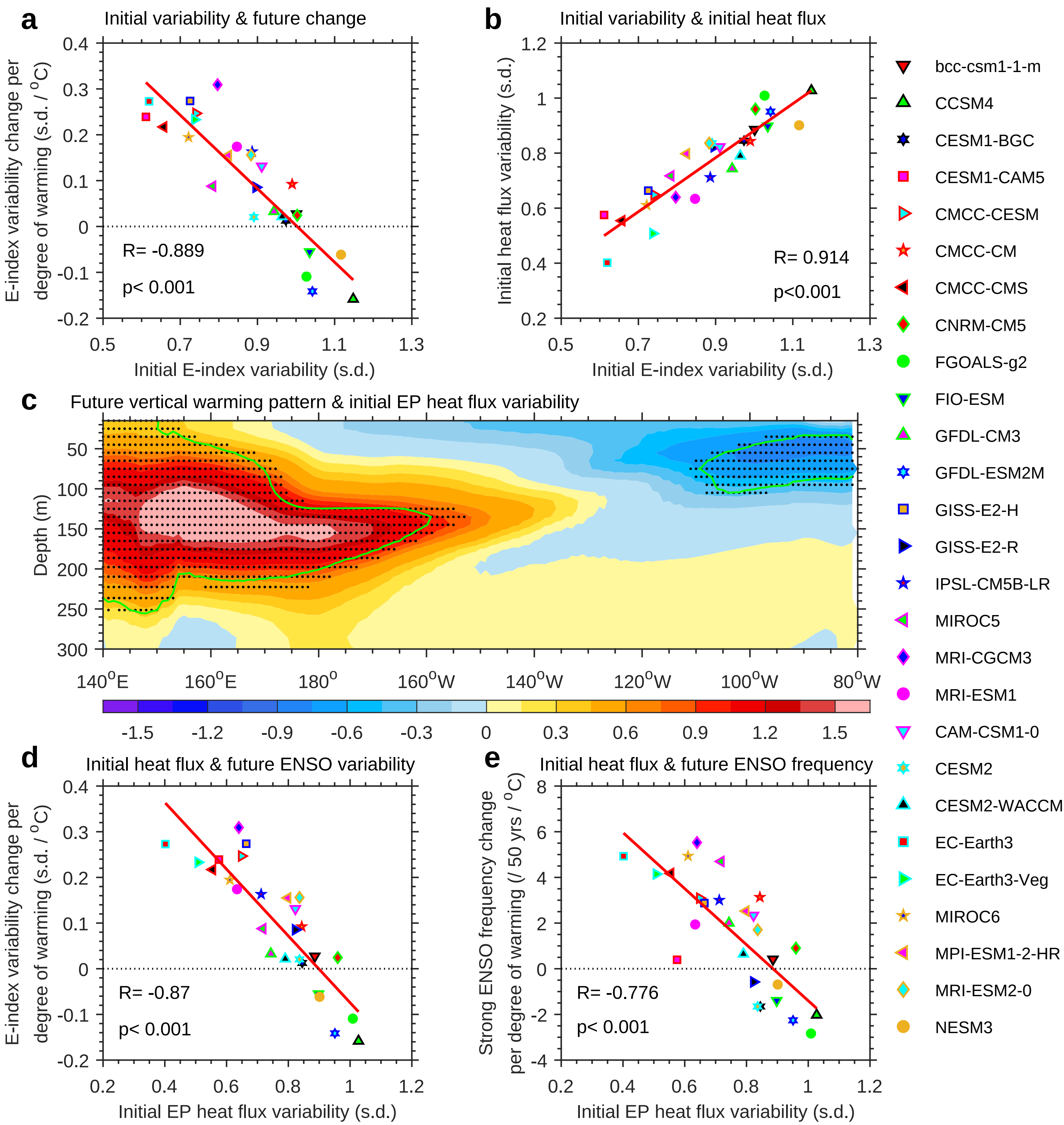

a
Initial variability & future change
E-index variability change per degree of warming (s.d. / °C)
Initial E-index variability (s.d.)
R= -0.889
p< 0.001
b
Initial variability & initial heat flux
Initial heat flux variability (s.d.)
Initial E-index variability (s.d.)
R= 0.914
p<0.001
c
Future vertical warming pattern & initial EP heat flux variability
Depth (m)
140°E
160°E
180°
160°W
140°W
120°W
100°W
80°W
-1.5
-1.2
-0.9
-0.6
-0.3
0
0.3
0.6
0.9
1.2
1.5
d
Initial heat flux & future ENSO variability
E-index variability change per degree of warming (s.d. / °C)
Initial EP heat flux variability (s.d.)
R= -0.87
p< 0.001
e
Initial heat flux & future ENSO frequency
Strong ENSO frequency change per degree of warming (/ 50 yrs / °C)
Initial EP heat flux variability (s.d.)
R= -0.776
p< 0.001
bcc-csm1-1-m
CCSM4
CESM1-BGC
CESM1-CAM5
CMCC-CESM
CMCC-CM
CMCC-CMS
CNRM-CM5
FGOALS-g2
FIO-ESM
GFDL-CM3
GFDL-ESM2M
GISS-E2-H
GISS-E2-R
IPSL-CM5B-LR
MIROC5
MRI-CGCM3
MRI-ESM1
CAM-CSM1-0
CESM2
CESM2-WACCM
EC-Earth3
EC-Earth3-Veg
MIROC6
MPI-ESM1-2-HR
MRI-ESM2-0
NESM3